# Effect of specimen orientation on the accuracy of vector field electron tomography

**Z. D. C. KEMP,**[1,*] **D. M. PAGANIN,**[1] **T. C. PETERSEN,**[1,2] **AND M. J. MORGAN**[1]

[1] *School of Physics and Astronomy, Monash University, Victoria 3800, Australia*
[2] *Monash Centre for Electron Microscopy, Monash University, Victoria 3800, Australia*
*[*]zachary.kemp@monash.edu*

**Abstract:** Vector field electron tomography (VFET) reconstructs vector fields based on phase maps recorded from two or more orthogonal tilt series. The tomographic reconstruction of vector fields involves considerations beyond those involved in the reconstruction of scalar fields. Here we examine the effect of initial magnetization orientation on reconstruction errors. The orientation of a magnetic particle affects the contrast in the phase maps. This, in turn, affects the accuracy of the reconstructed vector fields. We derive expressions that model the dependence of reconstruction errors on initial specimen orientation when using a filtered backprojection algorithm to reconstruct a vector potential from two tilt series. We compare these analytical results with those from numerical simulations. Our results can inform experimental procedures, such as sample preparation techniques and the choice of tilt series orientations. Specimen orientation can be a significant source of error in VFET, and our results can provide the means to minimize these errors.

## References and links

1. B. Poornaprakash, S. Sambasivam, D. Amaranatha Reddy, G. Murali, R. P. Vijayalakshmi, and B. K. Reddy, "Dopant induced RTFM and enhancement of fluorescence efficiencies in spintronic ZnS: Ni nanoparticles," Ceram. Int. **40**, 2677–2684 (2014).
2. L. Wu, J. Pierre-Olivier, D. Berman, W. Imaino, A. Nelson, H. Zhu, S. Zhang, and S. Sun, "Monolayer assembly of ferrimagnetic CoxFe3-xO4 nanocubes for magnetic recording," Nano Lett. **14**, 3395–3399 (2014).
3. E. A. Lee, H. Yim, J. Heo, H. Kim, G. Jung, and N. S. Hwang, "Application of magnetic nanoparticle for controlled tissue assembly and tissue engineering," Arch. Pharm. Res. **37**, 120–128 (2014).
4. Y. Murakami, T. Tanigaki, T. T. Sasaki, Y. Takeno, H. S. Park, T. Matsuda, T. Ohkubo, K. Hono, and D. Shindo, "Magnetism of ultrathin intergranular boundary regions in Nd–Fe–B permanent magnets," Acta Mater. **71**, 370–379 (2014).
5. R. P. Yu, M. J. Morgan, and D. M. Paganin, "Lorentz-electron vector tomography using two and three orthogonal tilt series," Phys. Rev. A **83**, 023813 (2011).
6. S. J. Lade, D. M. Paganin, and M. J. Morgan, "3-d vector tomography of doppler-transformed fields by filtered-backprojection," Opt. Commun. **253**, 382–391 (2005).
7. C. Phatak, M. Beleggia, and M. De Graef, "Vector field electron tomography of magnetic materials: Theoretical development," Ultramicroscopy **108**, 503–513 (2008).
8. A. G. Temiryazev, S. A. Saunin, V. E. Sizov, and M. P. Temiryazeva, "Magnetic force microscopy study of domain structures in magnetic films," B. Russ. Acad. Sci. Phys. **78**, 49–52 (2014).
9. V. Volkov and Y. Zhu, "Lorentz phase microscopy of magnetic materials," Ultramicroscopy **98**, 271–281 (2004).
10. E. M. Humphrey, "Three-dimensional magnetic field determination in magnetic nanoparticles using iterative reconstruction techniques," Ph.D. thesis, Carnegie Mellon University (2013).
11. S. J. Lade, D. M. Paganin, and M. J. Morgan, "Electron tomography of electromagnetic fields, potentials and sources," Opt. Commun. **253**, 392–400 (2005).
12. T. Tanigaki, Y. Takahashi, T. Shimakura, T. Akashi, R. Tsuneta, A. Sugawara, and D. Shindo, "Three-dimensional observation of magnetic vortex cores in stacked ferromagnetic discs," Nano Lett. **15**, 1309–1314 (2015).
13. Y. Aharonov and D. Bohm, "Further considerations on electromagnetic potentials in the quantum theory," Phys. Rev. **123**, 1511 (1961).
14. A. Tonomura, T. Matsuda, J. Endo, T. Arii, and K. Mihama, "Holographic interference electron microscopy for determining specimen magnetic structure and thickness distribution," Phys. Rev. B **34**, 3397–3402 (1986).
15. A. Kohn, A. K. Petford-Long, and T. C. Anthony, "Magnetic potential in patterned materials determined using energy-dependent lorentz phase microscopy," Phys. Rev. B **72**, 014444 (2005).

16. D. Paganin and K. A. Nugent, "Noninterferometric phase imaging with partially coherent light," Phys. Rev. Lett. **80**, 2586 (1998).
17. R. W. Gerchberg and W. O. Saxton, "Phase retrieval by iterated projections," Optik **35**, 237 (1972).
18. E. Snoeck, C. Gatel, L. M. Lacroix, T. Blon, S. Lachaize, J. Carrey, M. Respaud, and B. Chaudret, "Magnetic configurations of 30 nm iron nanocubes studied by electron holography," Nano Lett. **8**, 4293–4298 (2008).
19. M. Reed Teague, "Deterministic phase retrieval: a Green's function solution," J. Opt. Soc. Am. **73**, 1434–1441 (1983).
20. M. De Graef and Y. Zhu, "Quantitative noninterferometric Lorentz microscopy," J. Appl. Phys. **89**, 7177–7179 (2001).
21. C. Zuo, Q. Chen, Y. Yu, and A. Asundi, "Transport-of-intensity phase imaging using Savitzky-Golay differentiation filter - theory and applications," Opt. Express **21**, 5346–5362 (2013).
22. C. Phatak, "On the use of phase reconstructed vector field electron tomography for the three-dimensional study of magnetic materials," Ph.D. thesis, Carnegie Mellon University (2009).
23. D. Shindo and Y. Murakami, "Electron holography of magnetic materials," J. Phys. D Appl. Phys. **41**, 183002 (2008).
24. Z. D. C. Kemp, T. C. Petersen, D. M. Paganin, K. M. Spiers, M. Weyland, and M. J. Morgan, "Analysis of noise-induced errors in vector-field electron tomography," Phys. Rev. A **90**, 023859 (2014).
25. T. E. Gureyev and K. A. Nugent, "Rapid quantitative phase imaging using the transport of intensity equation," Opt. Commun. **133**, 339–346 (1997).
26. M. Pavel, G. Sperling, T. Riedl, and A. Vanderbeek, "Limits of visual communication: the effect of signal-to-noise ratio on the intelligibility of American Sign Language," J. Opt. Soc. Am. A **4**, 2355–2365 (1987).
27. E. Peli, "Contrast in complex images," J. Opt. Soc. Am. A **7**, 2032–2040 (1990).
28. D. Paganin, A. Barty, P. J. McMahon, and K. A. Nugent, "Quantitative phase-amplitude microscopy. III. the effects of noise," J. Microsc-Oxford **214**, 51–61 (2004).
29. M. Beleggia and Y. Zhu, "Electron-optical phase shift of magnetic nanoparticles I. basic concepts," Philos. Mag. **83**, 1045–1057 (2003).
30. E. J. Kirkland, *Advanced Computing in Electron Microscopy* (Springer, 2010), Chap. 3.

## 1. Introduction

Magnetic nanomaterials are of interest in many areas of materials science and condensed matter physics. Examples exist in such diverse fields as spintronics [1], magnetic information storage [2], biomedical engineering [3], and the study of nanoscale grain boundaries in hard magnets [4]. In order to fully characterize these materials, it is essential to have techniques to accurately measure their magnetic properties at the nanoscale. Vector field electron tomography (VFET) is a method for the characterization of such magnetic nanomaterials [5–7]. It has significant advantages over other methods used to characterize magnetic nanomaterials. Unlike magnetic force microscopy [8], it can reconstruct vector fields *inside* the specimen as well as on the surface, and unlike conventional Lorentz transmission electron microscopy [9], it reconstructs the vectors in three dimensions rather than only projections.

Tomography is the process of reconstructing an object function from its projections. These projections are recorded at multiple angles, as one or more tilt series, by rotating the specimen relative to the source and detector. The original function is then reconstructed from these tilt series, which can be achieved using a backprojection algorithm [6] or iterative reconstruction techniques [10]. Reconstruction of a three-dimensional vector field requires at least two tilt series [5]. In VFET, the tilt series are composed of phase maps which can be obtained using propagation based phase retrieval [11] or off-axis electron holography [12].

VFET can be used to reconstruct a variety of vector fields, such as the magnetic induction field, electric current density, and magnetic vector potential [11]. For this work, we consider only the reconstruction of the magnetic vector potential.

The defining feature of a vector field is that, in addition to its magnitude, it has a direction associated with each point in space. The magnitude of the projected vector potential, and hence the magnetic phase contrast, changes as the particle is rotated through at least one of the tilt series, regardless of the geometry of the specimen. Maximizing the average contrast can improve the reconstruction if errors in the retrieved phases are low, but can worsen its accuracy if errors in the retrieved phases are high. This results in errors in the reconstructed vector potential that depend on the initial orientation of the specimen relative to each tilt series. Additionally, the

Incident    Vector    Exit

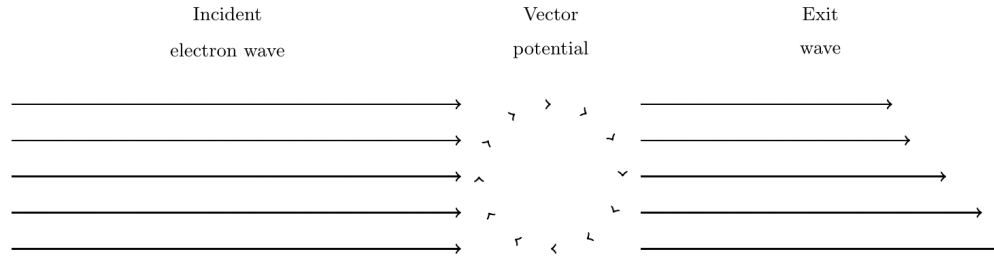electron wave    potential    wave

Fig. 1. Diagram showing the phase shift (represented by the length of the arrows) in the electron beam after passing through a magnetic vector potential.

optimum initial orientation can depend on factors such as attenuation and defocus, which affect the accuracy of the retrieved phases.

In this work, we quantify the effect that specimen orientation has on the resulting errors for a reconstruction algorithm utilizing two orthogonal tilt series. In Sec. 2 we review the theoretical basis for the VFET reconstruction process and our error analysis. In Sec. 3 we demonstrate how the concept of contrast can be used to quantify the error contribution from a single phase map due to specimen orientation. In Sec. 4 we use these results to derive equations that explain the changes in reconstruction error as a function of initial specimen orientation, and in Sec. 5 we present results of simulations which we compare with the analytical results. Some concluding remarks are given in Sec. 6.

## 2. Theoretical background

In the transmission electron microscope (TEM), the electron beam may be modeled as a complex scalar field (beam-like unbound wavefunction) that acquires a phase shift over planes perpendicular to the beam axis due to the Aharonov-Bohm effect as it traverses an electromagnetic specimen [13]. The phase, which is composed of an electrostatic part and a magnetic part, can be measured using electron holography, either in-line or off-axis, and additional measurements can be used to separate the two components [14, 15]. The principle of the magnetic Aharonov-Bohm effect is illustrated in Fig. 1.

VFET reconstructs vector fields from phase maps recorded for multiple angles over at least two orthogonal tilt series [5]. The phase maps, which correspond to the exit phase of the electron wavefunction, can be obtained via any of a number of phase reconstruction methods, including linear [16] and iterative [17] propagation based (in-line) methods, as well as off-axis [18] holographic techniques. We use a propagation based method, reconstructing the exit phase from out-of-focus micrographs using the transport of intensity equation (TIE) [16, 19]. In our numerical work, we simulate one over- and one underfocused micrograph for each angle in each tilt series, and approximate the in-focus micrograph from the two out-of-focus micrographs. After retrieving the phase from the simulated micrographs and separating the magnetic and electrostatic components, we reconstruct the vector potential from the magnetic phase maps using a filtered backprojection algorithm. The remainder of this section will address these processes in greater detail.

The phase shift induced in the electron wavefunction due to the magnetic vector potential $\mathbf{A}(\mathbf{r}_\perp, z)$ is given by [19]

$$\varphi_m(\mathbf{r}_\perp) = -\frac{e}{\hbar} \int \mathbf{A}(\mathbf{r}_\perp, z) \cdot d\mathbf{z}, \tag{1}$$

where $z$ is the electron propagation direction, $\mathbf{r}_\perp$ is the position vector in the plane orthogonal to $z$, $e$ is the magnitude of the electron's charge, and $\hbar$ is the reduced Planck constant. There is a corresponding electrostatic phase shift given by

$$\varphi_e(\mathbf{r}_\perp) = \frac{\pi}{E\lambda} \int V(\mathbf{r}_\perp, z)dz, \tag{2}$$

where $E$ is the accelerating potential of the TEM, $\lambda$ is the electron wavelength, and $V$ is the electrostatic potential of the specimen. The total phase shift is then given by

$$\varphi = \varphi_e + \varphi_m. \tag{3}$$

In scalar electron tomography utilizing electron intensities, the projection requirement limits analyses to weakly scattering specimens. In comparison, the electron holography aspect of VFET ensures applicability to strong scatterers and the reconstruction of electromagnetic properties. To obtain $\varphi$ from defocused non-interferometric intensity measurements alone, we employ a phase retrieval method based on the TIE, which relates transverse derivatives of the phase to the longitudinal derivative of the intensity [16, 19, 20]:

$$-k\frac{\partial I_0}{\partial z} = \nabla_\perp \cdot (I_0 \nabla_\perp \varphi_0). \tag{4}$$

Here $k$ is the electron wave number, $I_0$ and $\varphi_0$ are the intensity and phase at the image plane, respectively, $\nabla_\perp$ is the two-dimensional gradient operator over $\mathbf{r}_\perp$, and

$$\frac{\partial I_0}{\partial z} \equiv \left.\frac{\partial I(\mathbf{r}_\perp, z)}{\partial z}\right|_{z=0}. \tag{5}$$

In our reconstructions, the derivative of the intensity is obtained using a two-image central difference approximation given by [21]

$$\frac{\partial I_0}{\partial z} \approx \frac{I^+ - I^-}{2\Delta f}, \tag{6}$$

where $\Delta f$ is the defocus, and $I^+$ and $I^-$ are the over- and under-focus intensities, respectively. We calculate the in-focus micrograph using the approximation

$$I_0 \approx \frac{I^+ + I^-}{2}, \tag{7}$$

and solve Eq. (4) for $\varphi_0$ using a Fourier transform method [16, 22]:

$$\varphi_0 = -\frac{k}{4\pi^2}\mathcal{F}^{-1}\left\{\frac{\mathbf{k}}{|\mathbf{k}|^2} \cdot \mathcal{F}\left\{\frac{1}{I_0}\mathcal{F}^{-1}\left\{\mathcal{F}\left\{\frac{\partial I_0}{\partial z}\right\}\frac{\mathbf{k}}{|\mathbf{k}|^2}\right\}\right\}\right\}, \tag{8}$$

where $\mathbf{k}$ is the wave vector.

The magnetic component of the phase can be obtained via any of several methods [23]. In this work, $\varphi_m(\mathbf{r}_\perp)$ is obtained from the exit phase $\varphi(\mathbf{r}_\perp)$ using the time-reversal property [7]

$$\varphi_m = \frac{\varphi - \varphi'}{2}, \tag{9}$$

where $\varphi'$ is the phase obtained by rotating the specimen by 180° about an axis orthogonal to $z$ and reflecting the resulting phase map in this axis. By retrieving $\varphi_m$ for multiple orientations, the tilt series [5]

$$T^\theta(x, z) = -\frac{\hbar}{e}\varphi_m(x, z, \theta), \tag{10}$$

and

$$T^{\alpha}(y, x) = -\frac{\hbar}{e}\varphi_m(y, x, \alpha),\tag{11}$$

are constructed. Here, $\theta$ and $\alpha$ indicate positive angles of rotation about the $z$ and $x$ axis, respectively. We then reconstruct the vector potential, in the Coulomb gauge, using a filtered backprojection algorithm given by [5]

$$\mathbf{A}(x, y, z) = \int_0^{\pi}\int_{-\infty}^{\infty}\int_{-\infty}^{\infty}\frac{\tilde{T}^{\theta}|k_r^{\theta}|k_r^{\theta}}{k_x^2 + k_y^2 + k_z^2}\begin{bmatrix}\frac{k_y^2+k_z^2}{k_y}\\-k_x\\\frac{k_x k_z}{k_y}\end{bmatrix}e^{2\pi i[k_r^{\theta}(x\cos\theta+y\sin\theta)+k_z z]}\mathrm{d}k_r^{\theta}\mathrm{d}k_z\mathrm{d}\theta$$

$$+\int_0^{\pi}\int_{-\infty}^{\infty}\int_{-\infty}^{\infty}\frac{\tilde{T}^{\alpha}|k_r^{\alpha}|k_r^{\alpha}}{k_x^2 + k_y^2 + k_z^2}\begin{bmatrix}\frac{k_x k_z}{k_y}\\k_z\\\frac{-k_x^2-k_y^2}{k_y}\end{bmatrix}e^{2\pi i[k_r^{\alpha}(y\cos\alpha+z\sin\alpha)+k_x x]}\mathrm{d}k_r^{\alpha}\mathrm{d}k_x\mathrm{d}\alpha.$$

$$\tag{12}$$

Here, $k_x$, $k_y$, and $k_z$ are the Fourier space coordinates corresponding to the real space coordinates $x$, $y$, and $z$, respectively. Fourier transformed quantities are indicated with tildes, and $k_r^{\theta} = k_y/\sin\theta$ and $k_r^{\alpha} = k_y/\cos\alpha$ are radial spatial frequencies.

## 3. Orientation dependent errors

In VFET, magnetic phase contrast in the micrographs is the source of the information that is used to reconstruct the vector field. Because the projection of the magnetic vector potential changes with specimen orientation, the magnetic phase contrast varies as the specimen is rotated through each tilt series. The phase maps used in the filtered backprojection reconstruction algorithm (Eq. (12)) are not uniformly distributed over the sphere. Because of this, the average magnetic phase contrast can vary with initial orientation of the specimen.

If the errors in the phase maps are small, maximizing the average contrast in the micrographs minimizes the error in the reconstruction. However, when the errors are significant (e.g., for large defocus), the increased contrast results in an increase in the reconstruction error.

In the remainder of this section, we describe the choice of coordinate system used for the error analysis, and discuss these competing sources of orientation dependent errors.

### 3.1. Coordinate system used in the error analysis

In our simulations, the two tilt series are acquired as the specimen is rotated around the $x$- and $z$-axes, respectively. Consequently, it is natural to use spherical coordinates with the pole aligned with the $-y$ direction for describing the magnetization direction. In this work, we define our coordinate system such that the polar angle is given by

$$\gamma = \arccos\left(\frac{-y}{\sqrt{x^2 + y^2 + z^2}}\right),\tag{13}$$

and the azimuthal angle is given by

$$\gamma' = \arctan\left(\frac{z}{x}\right).\tag{14}$$

The geometry of the tilt series acquisition, as well as the corresponding coordinate system given by Eqs. (13) and (14), is shown in Fig. 2. For consistency with previous work [5, 24],
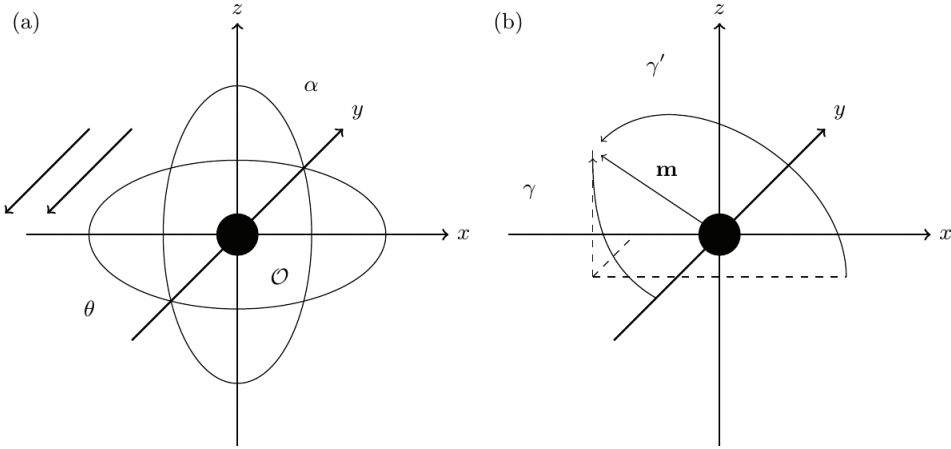
Fig. 2. (a) Geometry used for the acquisition of tilt series. In the $\alpha$ series, the object $\mathcal{O}$ is rotated about the $x$-axis and, in the $\theta$ series, it is rotated about the $z$-axis. (b) Spherical polar coordinate system used to describe magnetization directions. Here $\mathbf{m}(\gamma, \gamma')$ is the magnetization vector of the particle, which is assumed to be uniformly magnetized, $\gamma$ is the polar angle measured from the negative $y$-axis, and $\gamma'$ is the azimuthal angle, measured from the $x$-axis to the projection of $\mathbf{m}$ onto the $x - z$ plane.

the reconstruction algorithm we use involves a different electron propagation direction for each of the tilt series, but for visual clarity, we show only one direction in our diagrams. The two methods are equivalent, amounting only to a different start and end point in the $\alpha$ tilt series. Note, also, that the chosen coordinate system for the tilt series acquisition is arbitrary, and our analysis is valid for any reconstruction using two orthogonal tilt series, provided that $\gamma$ and $\gamma'$ are defined relative to the orientation of the tilt series in the given coordinate system.

### 3.2. Image contrast as a source of error

In vector tomography, for each vector in the field to be reconstructed, there are orientations for which this vector contributes no contrast in the projection. Specifically, for a dipole, the image contrast vanishes if the moment direction is parallel to the optic axis of the TEM, and contributes the maximum possible contrast if it is orthogonal. In the remainder of this section, we derive an expression for the magnetic phase contrast in terms of moment orientation for a dipole, which we use in Sec. 4 to obtain an expression for the root-mean-square (rms) reconstruction error in terms of the magnetization direction.

The phase object approximation is valid when the electron wavelength is significantly shorter than the characteristic length scale of the sample [5]. Under this approximation, $I_0$ is constant, and Eq. (4) becomes [25]

$$-k\frac{\partial I_0}{\partial z} = I_0 \nabla_\perp^2 \varphi_0. \tag{15}$$

Utilizing a forward difference approximation for $\partial I / \partial z$, the TIE under the phase object approximation can be written

$$\frac{I^+ - I_0}{\Delta f} = -\frac{I_0}{k}\nabla_\perp^2 \varphi_0. \tag{16}$$

This gives us an expression for the overfocused intensity:

$$I^+ = -\frac{I_0 \Delta f}{k} \nabla_\perp^2 \varphi_0 + I_0. \tag{17}$$

For our purposes, we use the rms definition of contrast [26, 27]. In the context of VFET, we are concerned with the rms contrast in the magnetic component of the defocused micrographs, which is given by

$$K = \sqrt{\frac{1}{I_0^2(M^2-1)} \sum_{i,j} \left(I_{i,j}^+ - I_0\right)^2} \tag{18}$$

$$= \sqrt{\frac{1}{(M^2-1)} \sum_{i,j} \left[\frac{\Delta f}{k} \nabla_\perp^2 (\varphi_m(\mathbf{r}_\perp))\right]^2}, \tag{19}$$

where $M$ is the width of the micrograph in pixels. Here, we have made use of the fact that, under the phase object approximation, $I_0$ is a constant, and is equal to the mean value of $I^+$. We have also discarded the electrostatic component of $\varphi_0$ because we are only interested in modeling the behavior of the *magnetic* contrast. In our simulations, we separate the two components using the time-reversal property (Eq. (9)); for the purposes of this analysis, we assume this separation to be perfect.

The phase shift induced in the electron wavefunction by a magnetic dipole is given by

$$\varphi_m = -\frac{e}{\hbar} \int \mathbf{A} \cdot d\mathbf{z} = -\frac{\mu_0 e}{2\pi\hbar} \frac{(\mathbf{m} \times \mathbf{r}) \cdot \hat{\mathbf{z}}}{x^2 + y^2}, \tag{20}$$

where $\mu_0$ is the permeability of free space, and $\mathbf{m}$ is the magnetic dipole moment. Note that the dot product here acts as an implicit projection, removing the z-dependence of $\mathbf{m} \times \mathbf{r}$. Eq. (20) describes the phase shift of an infinitesimal magnetization density, and the Laplacian of $\varphi_m$ vanishes. To model the magnetic phase contrast arising from a small, but finite, uniformly magnetized particle, we add a regularization parameter $\tau$ to the analytic form of the phase, giving

$$\nabla^2 (\varphi_m) = -\frac{\mu_0 e}{2\pi\hbar} \nabla_\perp^2 \left(\frac{(\hat{\mathbf{z}} \times \mathbf{m}) \cdot \mathbf{r}}{x^2 + y^2 + \tau^2}\right) \tag{21}$$

$$= \frac{4\mu_0 e}{\pi\hbar} \left(\tau^2 \frac{(\hat{\mathbf{z}} \times \mathbf{m}) \cdot \mathbf{r}}{(x^2 + y^2 + \tau^2)^3}\right), \tag{22}$$

where $\mathbf{r} \equiv (x, y, z)$ is the position vector. In terms of the magnetization, utilizing Eqs. (19) and (22), the contrast is given by

$$K = \frac{4\mu_0 e \Delta f |\mathbf{m}|}{\pi\hbar k \sqrt{M^2-1}} \sqrt{\sum_{i,j} \left(\tau^2 \frac{(\hat{\mathbf{z}} \times \hat{\mathbf{m}}) \cdot \mathbf{r}}{(x^2 + y^2 + \tau^2)^3}\right)^2} \tag{23}$$

$$= \frac{4\mu_0 e \tau^2 \Delta f |\mathbf{m}||\hat{\mathbf{z}} \times \hat{\mathbf{m}}|}{\pi\hbar k \sqrt{M^2-1}} \sqrt{\sum_{i,j} \left(\frac{\cos \zeta}{(x^2 + y^2 + \tau^2)^3}\right)^2}, \tag{24}$$

where $\zeta$ is the angle between $\hat{\mathbf{z}} \times \hat{\mathbf{m}}$ and $\mathbf{r}_\perp$. Because the contrast is low far away from the dipole, we can approximate Eq. (24) by constraining the summation to a circular region of radius $M/2$ pixels. Under this approximation, $\cos^2 \zeta$ takes on all values in the range $[0, 1]$, irrespective of the direction of $\mathbf{m}$, and we can write

$$K \propto |\hat{\mathbf{z}} \times \hat{\mathbf{m}}|. \tag{25}$$

In this work, we use a normalized error metric to quantify the accuracy of the reconstructed vector potential, and expect this to be a function of the fractional rms contrast $K/K_{\max}$, where $K_{\max}$ is the maximum value $K$ can take as we vary $\hat{\mathbf{m}}$, i.e., the value of $K$ with $|\hat{\mathbf{z}} \times \hat{\mathbf{m}}| = 1$. Using Eq. (25), we can then express the fractional mean square contrast as

$$\frac{K^2}{K_{\max}^2} = |\hat{\mathbf{z}} \times \hat{\mathbf{m}}|^2 \tag{26}$$

$$= 1 - (\hat{\mathbf{m}} \cdot \hat{\mathbf{z}})^2. \tag{27}$$

### 3.3. Truncation error due to the finite difference approximation

In order to calculate the longitudinal derivative of the intensity for use in the TIE, a finite difference approximation must be employed. This results in a truncation error in the derivative, which contributes errors to the retrieved phases and, ultimately, to the reconstructed vector fields. To first order, the truncation error arising from the use of Eq. (6) is [28]

$$^{\mathrm{trunc}}E \approx \frac{(\Delta f)^2}{6} \frac{\partial^3 I_0}{\partial z^3}. \tag{28}$$

This implies that the mean square error in the phase map due to this contribution will be approximately a function of $(\Delta f)^4$.

## 4. Derivation of error estimates

In determining the vector potential of a specimen, the accuracy of a reconstruction method can be quantified in different ways depending on what properties of the specimen are of most interest. For this work, we use a normalized rms error defined by [5]

$$^{\mathrm{rms}}E = \sqrt{\frac{\sum_{i,j,k} |\mathbf{A}_{i,j,k}^{\mathrm{rec}} - \mathbf{A}_{i,j,k}|^2}{\sum_{i,j,k} |\mathbf{A}_{i,j,k}|^2}}. \tag{29}$$

$$\tag{30}$$

Under the assumption that the rms error contribution $^{\mathrm{rms}}\bar{E}_\varphi$ of a single phase map is a function of contrast, we make use of Eqs. (27) and (28), and expand $^{\mathrm{rms}}\bar{E}_\varphi^2$ as a Taylor series about $1 - (\hat{\mathbf{m}} \cdot \hat{\mathbf{z}})^2 = 0$ and $(\Delta f)^4 = 0$:

$$
^{\mathrm{rms}}\bar{E}_\varphi^2 \left( (\hat{\mathbf{m}} \cdot \hat{\mathbf{z}})^2, (\Delta f)^4 \right) = E^2(1,0)
$$
$$
+ \frac{1}{2} \left[ \frac{\partial^2 (^{\mathrm{rms}}\bar{E}_\varphi^2)}{\partial p^2} \left( (\hat{\mathbf{m}} \cdot \hat{\mathbf{z}})^2 - 1 \right)^2 + 2 \frac{\partial^2 (^{\mathrm{rms}}\bar{E}_\varphi^2)}{\partial p \partial q} \left( (\hat{\mathbf{m}} \cdot \hat{\mathbf{z}})^2 - 1 \right) (\Delta f)^4 + \frac{\partial^2 (^{\mathrm{rms}}\bar{E}_\varphi^2)}{\partial q^2} (\Delta f)^8 \right],
$$
$$\tag{31}$$

where $p \equiv (\hat{\mathbf{m}} \cdot \hat{\mathbf{z}})^2$ and $q \equiv (\Delta f)^4$. Here, we have set the partial derivatives of first order to zero, because we expect extrema in the error function at $(\hat{\mathbf{m}} \cdot \hat{\mathbf{z}})^2 = 1$ and $(\Delta f)^4 = 0$. These two assumptions arise because orientations of extremal contrast coincide with extremal contributions to errors in the reconstruction, and because the error in the finite difference approximation of Eq.

(16) vanishes as $\Delta f \to 0$, respectively. We replace the partial derivatives in Eq. (31) with the constants

$$A = \frac{\partial^2}{\partial p^2}(^{\text{rms}}\bar{E}_{\varphi}^2), \; B = \frac{\partial^2}{\partial p \partial q}(^{\text{rms}}\bar{E}_{\varphi}^2), \text{ and } C = \frac{1}{2}\frac{\partial^2}{\partial q^2}(^{\text{rms}}\bar{E}_{\varphi}^2).$$ (32)

The mean square error in the phase is then given by

$$^{\text{rms}}\bar{E}_{\varphi}^2\left((\hat{\mathbf{m}} \cdot \hat{\mathbf{z}})^2, (\Delta f)^4\right) = {}^{\text{min}}E^2 + \left(B(\Delta f)^4 - A\right)(\hat{\mathbf{m}} \cdot \hat{\mathbf{z}})^2 - B(\Delta f)^4 + \frac{1}{2}A(\hat{\mathbf{m}} \cdot \hat{\mathbf{z}})^4 + C(\Delta f)^8,$$ (33)

where we have combined the constant terms via $^{\text{min}}E^2 = E^2(1,0) + \frac{1}{2}A$. In general, the error contribution of the respective tilt series can be different. We use the subscripts $\alpha$ and $\theta$ to denote the tilt series to which each error and undetermined constant belongs. Equation (33) then evaluates to

$$^{\text{rms}}\bar{E}_{\varphi}^2(\alpha, \gamma, \gamma') = (m_y \sin(\alpha) + m_z \cos(\alpha))^2(B_{\alpha}(\Delta f)^4 - A_{\alpha}) - B_{\alpha}(\Delta f)^4$$
$$+ \frac{A_{\alpha}}{2}(m_y \sin(\alpha) + m_z \cos(\alpha))^4 + C_{\alpha}(\Delta f)^8 + {}^{\text{min}}E_{\alpha}^2$$ (34)

and

$$^{\text{rms}}\bar{E}_{\varphi}^2(\theta, \gamma, \gamma') = (m_x \sin(\theta) + m_y \cos(\theta))^2(B_{\theta}(\Delta f)^4 - A_{\theta}) - B_{\theta}(\Delta f)^4$$
$$+ \frac{A_{\theta}}{2}(m_x \sin(\theta) + m_y \cos(\theta))^4 + C_{\theta}(\Delta f)^8 + {}^{\text{min}}E_{\theta}^2$$ (35)

for the respective tilt series. Here we have made use of the fact that the direction of the magnetic moment, in terms of our spherical polar coordinates, $\gamma$ and $\gamma'$, is given by

$$\hat{\mathbf{m}} = \sin\gamma\cos\gamma'\hat{\mathbf{x}} + \cos\gamma\hat{\mathbf{y}} + \sin\gamma\sin\gamma'\hat{\mathbf{z}}.$$ (36)

Integrating Eqs. (34) and (35) over the respective tilt series gives the mean square errors

$$^{\text{rms}}\bar{E}_{\alpha}^2 = \frac{\pi}{2}(m_y^2 + m_z^2)(B_{\alpha}(\Delta f)^4 - A_{\alpha}) - \pi B_{\alpha}(\Delta f)^4$$
$$+ \frac{3\pi A_{\alpha}}{16}(m_y^2 + m_z^2)^2 + \pi C_{\alpha}(\Delta f)^8 + \pi^{\text{min}}E_{\alpha}^2$$ (37)

and

$$^{\text{rms}}\bar{E}_{\theta}^2 = \frac{\pi}{2}(m_y^2 + m_x^2)(B_{\theta}(\Delta f)^4 - A_{\theta}) - \pi B_{\theta}(\Delta f)^4$$
$$+ \frac{3\pi A_{\theta}}{16}(m_y^2 + m_x^2)^2 + \pi C_{\theta}(\Delta f)^8 + \pi^{\text{min}}E_{\theta}^2.$$ (38)

The total reconstruction error due to this alignment is obtained by summing the square-roots of Eqs. (37) and (38):

$$^{\text{rms}}\bar{E} = {}^{\text{rms}}\bar{E}_{\alpha} + {}^{\text{rms}}\bar{E}_{\theta}$$ (39)

In our simulations, the error contributions from the two tilt series are similar, so we drop the $\alpha$ and $\theta$ subscripts to reduce the number of unknown constants to a total of four.

## 5. Numerical simulations

The error estimate derived in Sec. 4 assumes the object to be dipole-like (small and uniformly magnetized). To test our analytical predictions for a realistic specimen, we compute micrographs from a simulated, uniformly magnetized magnetite specimen. The simulations begin with a sample mask representing a region of constant magnetization and electrostatic potential. For our simulations, we use a spherical sample mask with a diameter of $d = 100$ nm, centered at the origin. This shape is chosen to decouple the magnetization orientation from the specimen geometry. A Fourier transform method [29] is used to construct the vector potential from the sample mask. The projected potentials are calculated by integrating the magnetic vector potential and the electrostatic potential in the electron propagation direction, and attenuation is modelled in the simulations by including an imaginary component in the electrostatic potential. The exit phase is a linear combination of these projected potentials due to the Aharonov-Bohm phase shifts given in Eqs. (1) and (2). The out-of-focus micrographs are then computed by employing a transfer function formalism (see, for example, Ref. [30]).

A Fourier transform solution to the TIE [16] is used to retrieve the phase from the simulated micrographs, and a time-reversal method [14] is employed to recover its magnetic component. We reconstruct the magnetic vector potential of the simulated object using a filtered backprojection algorithm given by Eq. (12). Slices of the vector potential—exact, and reconstructed from samples with $\gamma = 0$ and $\gamma = \pi/2$, respectively—are shown in Fig. 3. Note that, unlike similar artefacts that occur in scalar tomography, the orientation-dependent streaking in these images cannot be easily removed using *a priori* knowledge, such as compact support of the specimen, because the electromagnetic fields of interest are non-trivial and extend outside specimen boundaries. The reconstruction error is then calculated using the rms metric defined in Eq. (29). For a given defocus, we vary the magnetization direction over 11 polar angles and 21 azimuthal angles, a total of 191 orientations of the magnetization, and perform the entire simulation and reconstruction process once for each orientation. This gives us the error as a function of specimen orientation. We compare these simulations with our analytical results based on Eqs. (37)–(39). The results for a single defocus are shown as grayscale plots in Fig. 4.

There are various numerical errors that affect the simulations for some parameter combinations. This includes sampling errors and wraparound artefacts. These errors are difficult to quantify, and the sampling would typically be high in experimental tomography. The wraparound effects are a numerical artefact, and do not occur in experimental micrographs. For these reasons we avoid these errors in our simulations, via an appropriate choice of image resolution and domain size, and focus on the error sources that are addressed by our analysis; namely, contrast dependent errors and truncation errors in the finite difference approximation (Eq. (6)) used for the TIE.

Our results, both simulated and analytical, for four different defoci, are presented as two dimensional scatter plots in Fig. 5.

Provided that a small number of unknowns is appropriately chosen, the analytical results for the rms error agree well with the simulations. In the results we present here, the optimal value for $\gamma$ is always $(\gamma \bmod \pi) = 0$. However, we have also performed simulations using smaller particles ($d = 40$ nm) and found that the optimum orientation can be $\gamma = \pi/2$ for small defocus, but changes to $(\gamma \bmod \pi) = 0$ above some critical defocus value. For large defocus, our results indicate that the optimal value is always $(\gamma \bmod \pi) = 0$. These results are consistent with our assertion that improved contrast reduces $^{\mathrm{rms}}E$ when the error in the retrieved phase is low. For a larger particle such as the $d = 100$ nm sphere, additional errors in the phase, due to increased attenuation, result in an increase in error with increasing contrast, even for small $\Delta f$. We have not included the results of the 40 nm particle simulations because of concerns that they may not be physically accurate due to the omission of superparamagnetic effects in any of our simulations.

The optimal azimuthal angle is difficult to predict, as it can be highly sensitive to small differences in the errors arising from each tilt series. However, in most cases the reconstruction
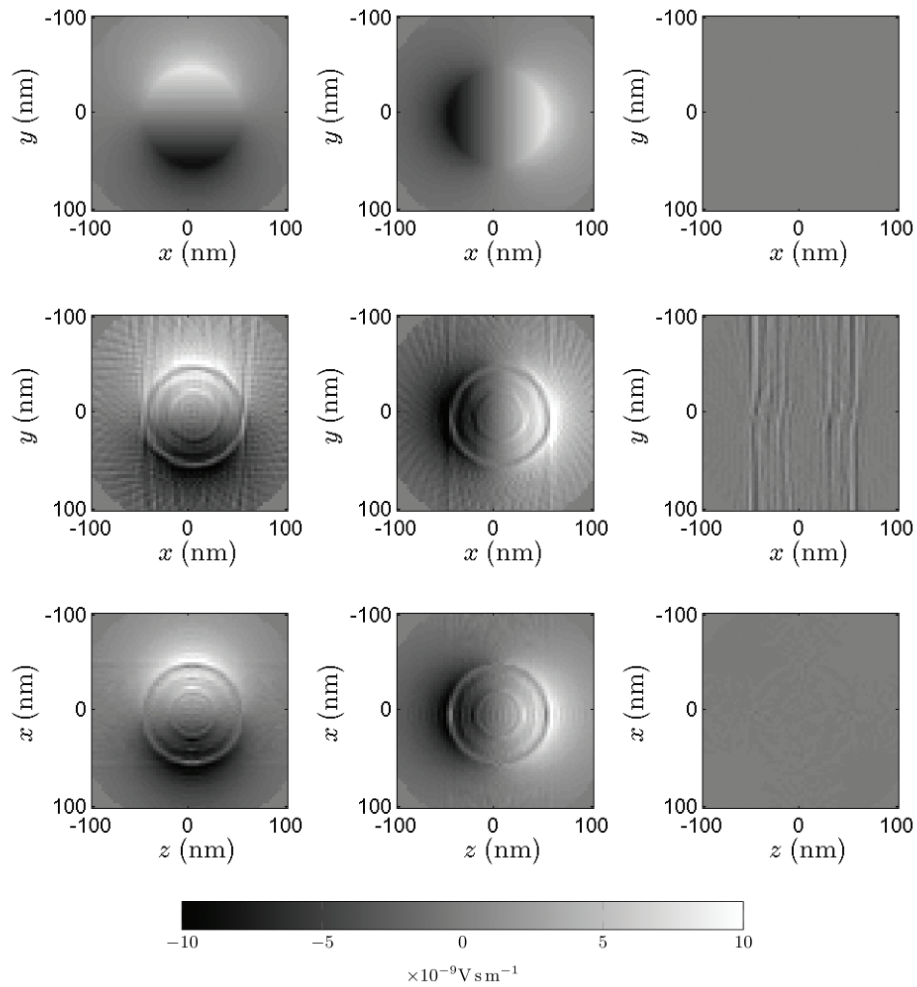
Fig. 3. A 1 voxel (3.125 nm) thick slice through the origin of each component of **A** for a 100 nm diameter magnetite sphere reconstructed from simulated micrographs with a defocus of 100 $\mu$m. Top row: The exact simulated vector potential. Middle row: Reconstruction with $\mathbf{m}(\gamma, \gamma')$ chosen to maximize $^{\mathrm{rms}}E$. Bottom row: Reconstruction with $\mathbf{m}(\gamma, \gamma')$ chosen to minimize $^{\mathrm{rms}}E$.

error is approximately constant with respect to $\gamma'$, and can be treated as such for the purposes of determining the ideal initial orientation of the specimen.
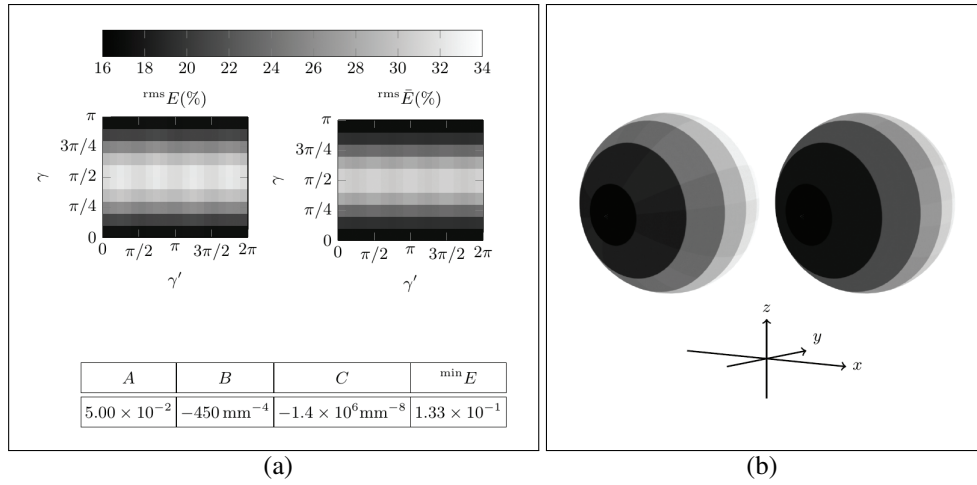
Fig. 4. (a) Grayscale plots of error as a function of specimen orientation for the $\Delta f = 25\ \mu$m case, using simulations (left) and analytical results (right). The errors here are shown as a function of $\gamma$ and $\gamma'$, and the table shows the values chosen for each constant in the analytical model. (b) The spheres show the results mapped back onto spherical coordinates, with the axes underneath indicating the orientation of these spheres in Cartesian coordinates.
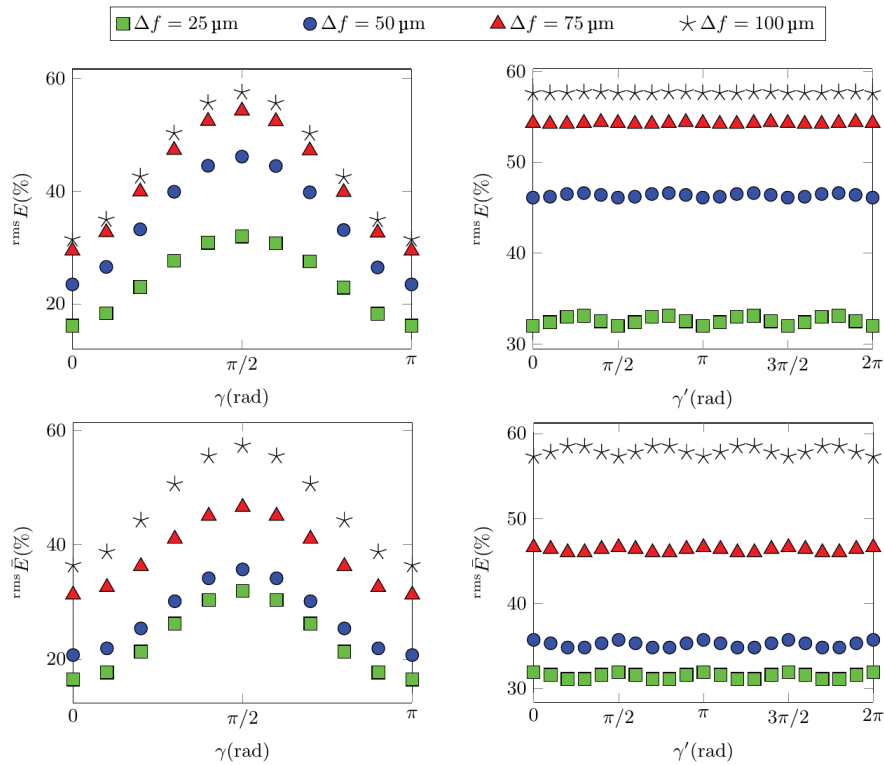


Fig. 5. Scatter plots showing the rms errors in the reconstructed vector potential as a function of initial specimen orientation and for a range of defoci, using simulated micrographs (top) and the analytical estimate (bottom). Plots on the left and right show slices at $\gamma' = 0$ and $\gamma = \pi/2$, respectively. For each defocus, in these results, the rms error varies by an approximate factor of two as a function of $\gamma$.

## 6.   Conclusion

The accuracy of VFET reconstructions exhibits a strong dependence on the initial orientation of the sample relative to the reconstruction geometry. The form of this dependence is easily estimated for the case where the object is uniformly magnetized. For many real-world materials, there is no such straightforward way of calculating these errors. However, many materials of interest exhibit a strong net magnetization and exhibit similar properties to a magnetic dipole, or uniformly magnetized particle.

When errors in the phase are high, as is the case when using a propagation based phase retrieval method with large defocus, or when there is significant attenuation, reconstruction errors can be reduced by orienting the particle such that the average magnetic phase contrast in the recorded micrographs is minimized. Conversely, if errors in the retrieved phase can be kept small, maximizing the average contrast reduces the total reconstruction error.

Where sample preparation techniques allow for the choice of magnetization orientation, reconstruction errors can be reduced by taking the effect of initial orientation into consideration.

## Funding